# UC Davis

## UC Davis Previously Published Works


### Title

Crystal structure, synthesis, and thermoelectric properties of Yb14ZnBi11


### Permalink

https://escholarship.org/uc/item/2cd7n8h0



### Journal

Journal of Materials Chemistry A, 14(60)

### ISSN

2050-7488



### Authors

Islam, MM

Opara, IC

Ruiz, CM

et al.



### Publication Date

2026-10-08

### DOI

10.1039/d6ta04884f



### Copyright Information

This work is made available under the terms of a Creative Commons Attribution License, available at https://creativecommons.org/licenses/by/4.0/

Peer reviewed

eScholarship.org Powered by the California Digital Library
University of California

# Crystal Structure, Synthesis, and Thermoelectric Properties of $Yb_{14}ZnBi_{11}$

Md. Minhajul Islam,[1] Ivan Chinonso Opara,[1] Christopher Miramontes Ruiz,[1] Yixuan Xu,[1] James C. Fettinger,[1] Svilen Bobev,[2] and Susan M. Kauzlarich[1*]

[1]Department of Chemistry, University of California, One Shields Ave, Davis, CA 95616, United States

[2]Department of Chemistry & Biochemistry, University of Delaware, Newark, Delaware 19716, United States

*Corresponding author: smkauzlarich@ucdavis.edu

## Abstract

Zintl compounds with the $Ca_{14}AlSb_{11}$ (14-1-11) structure have attracted attention for their excellent thermoelectric properties at high temperatures. They exhibit very low thermal conductivity, owing to their structural complexity, large unit cells, and the presence of heavy atoms. However, few bismuth-containing 14-1-11 compounds have been reported and investigated for their thermoelectric properties. In this work, a new member of this family, $Yb_{14}ZnBi_{11}$, has been synthesized as single crystals using the lead-flux method. The crystal structure was determined by single-crystal diffraction, confirming that it belongs to the $Ca_{14}AlSb_{11}$ structure type, with the tetragonal space group $I4_1/acd$ (No. 142; Z = 8). The unit cell parameters (90 K) are $a$ = 16.9937(6) Å, $c$ = 22.1377(11) Å, and $V$ = 6393.1(6) Å$^3$ [$R_1$ = 0.0269, $wR_2$ = 0.0553]. The formula unit contains fourteen $Yb^{2+}$ cations, one $[ZnBi_4]^{10-}$ tetrahedral unit, one polyanionic $Bi_3^{7-}$ unit, and four isolated $Bi^{3-}$ anions, making it a good candidate for achieving low thermal conductivity. Bulk polycrystalline $Yb_{14}ZnBi_{11}$ is synthesized for thermoelectric measurements, exhibiting a low thermal conductivity of 0.77 W m$^{-1}$ K$^{-1}$ at room temperature and a low electrical resistivity of 0.91 mΩ cm at 367 K. The potential of $Yb_{14}ZnBi_{11}$ for thermoelectric applications highlights the vast array of unexplored compounds available in this structure type for future research.

## 1 Introduction

Zintl phases are a class of compounds situated between intermetallic and insulating valence compounds, demonstrating potential in various energy applications.[1,2] These compounds have shown promise in thermoelectric devices,[3] batteries,[4] and photovoltaics.[5] According to the classical Zintl concept, electropositive elements formally donate their valence electrons to electronegative elements, allowing both to achieve filled valence shells.[6] This can result in salt-like ionic bonding between cations and anions in Zintl phases. In the optimized bonding scenario, bonding orbitals are occupied while antibonding orbitals remain unoccupied, making these compounds

semiconductors. However, in cases of electron deficiency, anionic units may form covalent bonds, leading to a combination of ionic and covalent bonding within the same phase. These semiconducting Zintl phases exhibit promising thermoelectric properties due to their small bandgap and low thermal conductivity, such as the "14-1-11" phase (e.g., $Eu_{14}GaAs_{11}$),[7] the "10-1-9" phase (e.g., $Ca_{10}AlSb_9$),[8] the "5-2-6" phase (e.g., $Sr_5In_2Sb_6$),[9] and the "11-4-2-12" phase (e.g., $Eu_{11}Zn_4Sn_2As_{12}$).[10,11] Furthermore, numerous stable Zintl phases with heavy elements and complex structures have been identified using machine learning (ML), highlighting their potential for thermoelectric applications.[12]

The Zintl 14-1-11 phase has exhibited impressive thermoelectric performance due to its low thermal conductivity and favorable electronic transport properties.[13] These compounds are generally denoted as $A_{14}MPn_{11}$, where $A$ represents a divalent alkali metal or a rare earth element; $M$ represents Mg, triels such as Al, Ga, In, and transition metals such as Mn, Fe, Zn, Cd; $Pn$ refers to pnictogens P, As, Sb, Bi. The structure can be explained using the Zintl concept, which describes it as valence-balanced: 14 $A^{2+}$ + $[MPn_4]^{9-}$ + $Pn_3^{7-}$ + 4 $Pn^{3-}$.[14] The polyanionic subunit $Pn_3^{7-}$ is best characterized by the presence of a split site for the central $Pn$ atom of the trimer for the lighter elements such as phosphorus and arsenic. In contrast, the splitting of the antimony site is only observed when large cations $A^{2+}$ are present. Compounds containing bismuth have yet to exhibit splitting in the polyanionic subunit. An ideal thermoelectric material would exhibit a high Seebeck coefficient, low electrical resistivity, and low thermal conductivity.[15] However, these properties are intricately linked to carrier concentration, making it challenging to simultaneously optimize all components to achieve a high thermoelectric figure of merit. Thus, materials with low thermal conductivity are promising candidates for exploring new thermoelectric materials.[16] 14-1-11 compounds have exhibited low thermal conductivity even in lighter arsenic- and antimony-containing compounds.[17,18] Moreover, the highly complex crystalline structure of 14-1-11 compounds leads to diffuson-driven lattice thermal conductivity.[19,20] As a result, low lattice thermal conductivity has also been observed in bismuth-containing 14-1-11 compounds, $Ca_{14}MgBi_{11}$,[21] $Sr_{14}MgBi_{11}$,[21] $Eu_{14}MgBi_{11}$,[21] $Yb_{14}MnBi_{11}$ and $Yb_{14}MgBi_{11}$.[22] Additionally, the lower electronegativity of bismuth leads to a smaller band gap, which could result in lower electrical resistivity.[17] Given these factors, $Yb_{14}ZnBi_{11}$ has the potential to demonstrate impressive thermoelectric performance at medium to high temperature ranges.[23] The performance of thermoelectric materials is quantified using the dimensionless figure of merit, denoted as $zT = S^2T/\kappa\rho$, where $S$ is the Seebeck coefficient, $\rho$ is the electrical resistivity, $\kappa$ is the total thermal conductivity, and $T$ is the absolute temperature. The total thermal conductivity is the sum of the lattice thermal conductivity and the electronic thermal conductivity.

In this work, the synthesis and crystal structure of a new bismuth-containing compound in the 14-1-11 family, $Yb_{14}ZnBi_{11}$, are presented. This compound adds to the 14-1-11 family, emphasizing the abundance of unexplored phases that could be the focus of future research. The structure determination reveals that $Yb_{14}ZnBi_{11}$ possesses all the characteristics typical of a 14-1-11 compound. A bulk polycrystalline sample of $Yb_{14}ZnBi_{11}$ was prepared using ball milling followed

by high-temperature annealing, and its thermoelectric properties were investigated. Measurements of the electronic transport properties show that this compound exhibits very low resistivity and metallic behavior as a function of temperature. Furthermore, the thermal transport properties indicate low lattice thermal conductivity, with a notable contribution from electronic thermal conductivity.

## 2 Experimental Section

### 2.1 Reagents

Elemental Yb pieces (Stanford Advanced Materials, 99.99%), Zn shot (Alfa Aesar, 99.95%), Bi shot (Alfa Aesar, 99.999%), and Pb shot (Alfa Aesar, 99.99%) were used for synthesis. Yb pieces were brushed to remove any surface oxide and cut into small pieces, and Zn, Bi, and Pb were used as received. All manipulations were carried out in an argon-filled glovebox with a moisture level < 0.5 ppm.

### 2.2 Single-Crystal Synthesis

The elements were loaded in a 5 mL alumina crucible with a frit disc and a catch crucible set with the ratio Yb:Zn:Bi:Pb = 14:6:11:86. The crucible assembly was further jacketed in a fused silica tube cushioned with silica wool at both top and bottom and sealed under ~1/4 atm Ar. The sealed reaction tube was placed upright in a box furnace, heated to 1100 °C for seven days, then cooled to 700 °C at 3.07 °C/hour. The reaction tube was removed, inverted, and centrifuged at 8500 rpm to separate the flux from the desired product. This reaction yielded $Yb_{14}ZnBi_{11}$ as the major product, in the form of small, faceted crystals sufficient to obtain crystallographic information by single-crystal analysis. In a glovebox equipped with a microscope, small black reflective crystals of $Yb_{14}ZnBi_{11}$ were selected, cut to the desired size, and transferred under Paratone oil to the diffractometer using MiTeGen micro-loops.

At the University of Delaware, samples containing single crystals of $Yb_{14}ZnBi_{11}$ were synthesized via several independent methods. Initially, multifaceted but poorly diffracting crystals of $Yb_{14}ZnBi_{11}$ were found among the products of reactions between Yb, Zn, and Bi aimed at $Yb_9Zn_{4+x}Bi_9$.[24] Equimolar amounts of Yb and Bi, together with a 20-fold excess amount of Zn (used as a flux), were used, and the reaction conditions from ref. 21 were adopted (heating to 960 °C, at a rate of 200 °C/h, held for 24 hours, and then cooled to 500 °C at a rate of 5 °C/h). Another set of experiments, this time using Pb as a flux, also yielded $Yb_{14}ZnBi_{11}$ crystals in small yields. These reactions between Yb, Zn, and Bi in molten Pb were attempts to extend the 21-4-18 chemistry and make $Yb_{21}Zn_4Bi_{18}$.[25] None of the products from the above-described experiments were single-phase materials, but, by their appearance, a few crystals were isolated and found to be consistent with the 14-1-11 structure type. Intensity data were collected, and the $Yb_{14}ZnBi_{11}$ crystal structure was established (CCDC #2558875). However, since Pb and Bi cannot be distinguished from X-ray diffraction, to fully validate the model, crystals of $Yb_{14}ZnBi_{11}$ were also obtained from a stoichiometric reaction between Yb, Zn, and Bi. The metals in the exact stoichiometric amounts

were loaded into 3/8” niobium tubes, which were then closed using an arc-welder. Consequently, the niobium tubes were placed inside fused silica ampoules and flame-sealed under high vacuum. Heating was conducted in a tube furnace, with the temperature being ramped up to 900 °C at a rate of 200 °C/h. The materials were then annealed for 96 hours. After this period, the temperature was gradually lowered to room temperature at a rate of 10 °C/h. While most of the crystalline material obtained was $Yb_{11}Bi_{10}$, several small crystals of $Yb_{14}ZnBi_{11}$ were also identified, and the crystal structure was refined again (CCDC #2558874).

### 2.3 Powder Synthesis

A polycrystalline sample of $Yb_{14}ZnBi_{11}$ was synthesized using a binary precursor through ball milling and high-energy annealing. Initially, the $Yb_5Bi_3$ binary phase was prepared by combining the required stoichiometric amounts of Yb pieces and Bi shot in a 65 $cm^3$ stainless-steel grinding vial. This mixture was ground with two stainless steel balls, each 12.7 mm in diameter, using a SPEX 8000D Mixer/Mill for 30 minutes. After the initial milling, the vial was scraped with a chisel and milled again in the machine for an additional hour. Once a homogeneous powder was obtained, it was loaded into an Nb tube and then jacketed inside a quartz tube under vacuum. The $Yb_5Bi_3$ phase was synthesized by annealing at 650 °C for 24 hours. For the ternary phase $Yb_{14}ZnBi_{11}$, stoichiometric amounts of $Yb_5Bi_3$, Zn, and Bi were loaded into a grinding vial. The $Yb_{14}ZnBi_{11}$ compound was synthesized using the same milling procedure described above, and then it was annealed at 800 °C for 96 hours.

### 2.4 Single-Crystal X-ray Diffraction

Single-crystal diffraction data were collected under a stream of cold nitrogen gas at 90 K on a Bruker Apex II diffractometer with a CCD detector with Mo Kα radiation (λ = 0.71073 Å). Four ω-scan data frame series were collected with 0.3° wide scans, 20 seconds per frame, and 565 frames collected per series at different φ angles (φ = 0°, 90°, 180°, 270°). The determination of unit cell parameters, refinements, and raw-frame data integration was completed using Bruker APEX III software. Space group determination was based on systematic absences using XPREP, and a semi-empirical absorption correction based on symmetrically equivalent reflections was applied using SADABS (CCDC #2557387).

At the University of Delaware, single-crystal X-ray diffraction data were collected at 200 K. This was done on a Bruker diffractometer with a CCD detector and monochromatic Mo Kα radiation (λ = 0.71037 Å). Data acquisition was managed by the Bruker APEX III software (CCDC #2558875, #2558874).

### 2.5 Powder X-ray Diffraction

Powder X-ray Diffraction (PXRD) data were collected at room temperature using a Bruker D8 ECO ADVANCE powder X-ray diffraction (PXRD) diffractometer on zero-background off-axis quartz plates. Cu Kα radiation was used with a step size of 0.02° over the 2θ angles of 20° to 80°.

### 2.6 Scanning Electron Microscopy (SEM) and Energy Dispersive X-ray Spectroscopy (EDS)

Scanning electron microscopy (SEM) was performed using a FEI Scios DualBeam FIB/SEM instrument, which is equipped with an Oxford Instruments X-Max 50 mm² silicon drift detector. The analysis was conducted at an accelerating voltage of 30 kV. Additionally, Energy Dispersive X-ray Spectroscopy (EDS) was used for elemental mapping with an Oxford X-Max Energy Dispersive X-ray Spectroscopy detector to provide detailed information on the elemental composition throughout the sample.

### 2.7 Spark Plasma Sintering

After sieving the powder sample through a 100-mesh screen, it was loaded into a 12.7 mm graphite die. Initially, the powder was cold-pressed at 5 kN using a Dr. Sinter Junior Spark Plasma Sintering system (Fuji Electronic Industrial Co., LTD) under Ar gas. The applied force was increased to 9 kN, and the powder was sintered at 900 °C for 30 minutes. The resulting pellets exhibited a density greater than 98%, measured by Archimedes' principle.

### 2.8 Thermal Transport Properties

Thermal diffusivity was measured on the pressed pellets using a Netzsch LFA 475 Microflash under Ar flow. A graphite coating was applied to the pellet surface to ensure maximum laser absorption. The total thermal conductivity was then calculated using the equation, $\kappa = D \times C_p \times \rho$. In this equation, $D$ represents the measured thermal diffusivity, $C_p$ denotes the heat capacity, and $\rho$ denotes the material's density. The heat capacity was approximated using the Dulong–Petit law.

### 2.9 Seebeck Coefficient and Electrical Resistivity

The Linseis LSR-3 instrument was utilized to measure the Seebeck coefficient and electrical resistivity of a bar that was cut from the pellet. For the measurements, Pt/Rh thermocouples were arranged in a four-probe configuration under a static helium atmosphere. Additionally, a polished zirconium ribbon was placed inside the susceptor to serve as an oxygen sponge, thereby protecting the sample’s integrity.

## 3 Results and Discussion

### 3.1 Structure

$Yb_{14}ZnBi_{11}$ belongs to the $Ca_{14}AlSb_{11}$ structure type and is similar to other 14-1-11 compounds that crystallize in the tetragonal space group $I4_1/acd$, as shown in **Fig. 1**. According to the Zintl formalism, the formula unit consists of fourteen $Yb^{2+}$ cations, one $[ZnBi_4]^{10-}$ tetrahedral unit, one polyanionic $Bi_3^{7-}$ unit, and four isolated $Bi^{3+}$ cations. However, this indicates that the phase is electron deficient. In the $Ca_{14}ZnSb_{11}$ phases, there is evidence of additional Zn interstitials in the antimonides.[14] Furthermore, these phases can be substituted with a trivalent rare earth element to achieve electron balance.[26] It is also possible to have an intermediate valence for both $Yb^{2+}$ and $Yb^{3+}$ in $Yb_{14}ZnBi_{11}$, similar to the behavior observed with the antimony analog.[27]. There are nine

independent crystallographic sites, eight formula units, and a total of 208 atoms in each unit cell. Due to the familiarity of this structure type, a detailed description is not provided here.[13] A brief overview highlighting the significant structural features will be discussed.

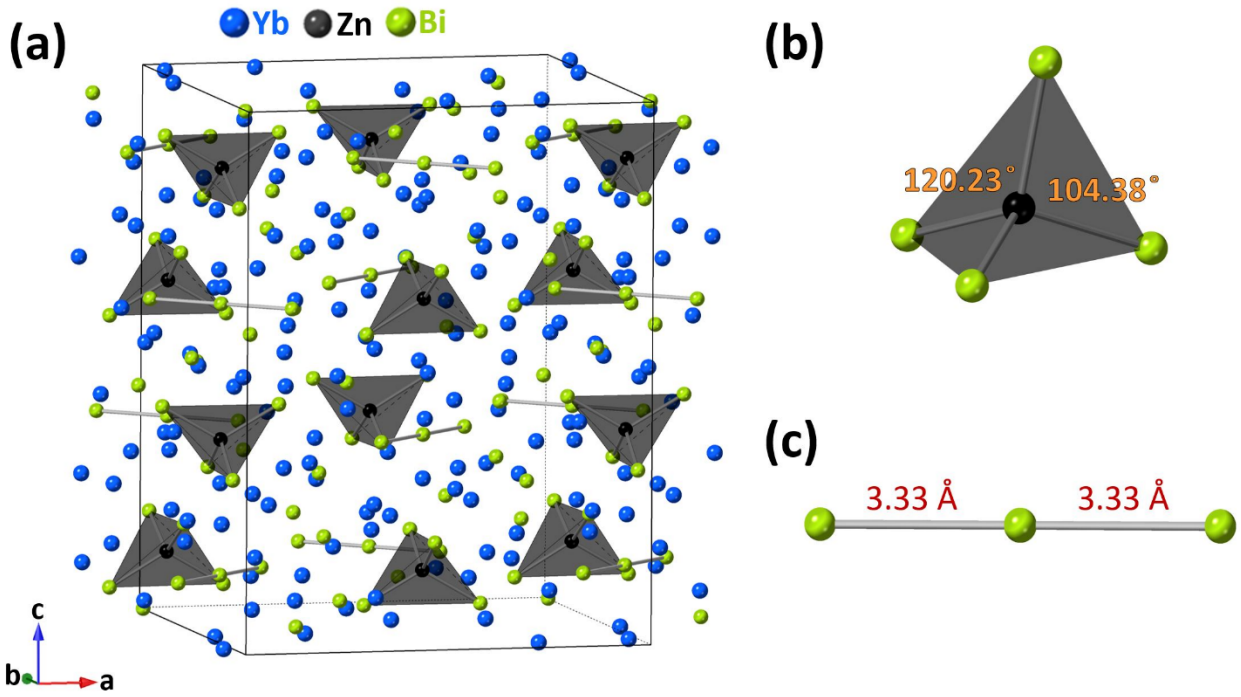



**Fig. 1** (a) The unit cell of $Yb_{14}ZnBi_{11}$. Yb, Zn and Bi atoms are represented by azure, black, and lime spheres. The $Bi_3^{7-}$ polyanionic subunit is shown with grey bonds, and the grey tetrahedra are isolated $[ZnBi_4]^{10-}$ units. (b) The compressed $[ZnBi_4]^{10-}$ tetrahedron bond angles. (c) The $Bi_3^{7-}$ three atom unit with bond lengths.

The unit-cell parameters (90(2) K for $Yb_{14}ZnBi_{11}$ are $a$ = 16.9937(6) Å, $c$ = 22.1377(11) Å, and $V$ = 6393.1(6) Å$^3$, typical of other Bi-containing 14-1-11 compounds. Detailed data collection and refinement parameters for flux-grown $Yb_{14}ZnBi_{11}$ at 90(2) K and 200(2) K are provided in **Table 1**. Fractional positional coordinates and isotropic thermal parameters for the atoms are provided in the Supplementary Information (**SI**), **Table S1**. Data collection parameters for the $Yb_{14}ZnBi_{11}$ crystal from a stoichiometric reaction of Yb, Zn, and Bi are also presented in the **SI**, **Table S2**. The lattice parameters of $Yb_{14}ZnBi_{11}$ are notably larger than those of its Sb analog, $Yb_{14}ZnSb_{11}$, which has $a$ = 16.562(3) Å, $c$ = 21.859(2) Å, and $V$ = 5995.9(16) Å$^3$.[28] It is notable that the size difference in the $M^{2+}$ ions affects the lattice parameters of these compounds. For example, the larger $Mn^{2+}$ ion, which has an ionic radius of 0.66 Å, leads to increased lattice parameters of $a$ = 17.000(3) Å, $c$ = 22.259(6) Å, and a volume of $V$ = 6433 (3) Å$^3$ in $Yb_{14}MnBi_{11}$.[29] However, although the ionic radius of $Mg^{2+}$ (0.57 Å) is slightly smaller than that of $Zn^{2+}$ (0.60 Å), the Mg-containing compound $Yb_{14}MgBi_{11}$ exhibits a larger lattice parameter, with $a$ = 16.974(2) Å, $c$ = 22.399(4) Å, and $V$ = 6454(2) Å$^3$ than the Bi containing $Yb_{14}ZnBi_{11}$.[30] This trend has also been observed for Mg and Zn

containing compounds of 14-1-11 arsenides and antimonides, as discussed by Islam et al. and Hu et al., respectively.[19,30] The $Yb_{14}ZnBi_{11}$ compound exhibits the smallest *c* lattice parameter and the lowest *c*/*a* ratio, indicating that it is more compressed along the *c*-axis compared to the Mg and Mn analogs. This difference in lattice parameters is attributed to variations in bond lengths and angles within the $[MBi4]^{10-}$ tetrahedral unit. **Table S3** presents the selected bond lengths and bond angles for $Yb_{14}ZnBi_{11}$ in the supplementary information (SI). Specifically, the bond length of Zn-Bi at 2.7901(5) Å is shorter than the bond length of Mg-Bi, which stands at 2.849(1) Å. This shorter bond length suggests the presence of covalent bonding within the tetrahedron formed between the metal center and the pnictogen. In addition, the bond angles of the tetrahedra in $Yb_{14}ZnBi_{11}$ are 104.375(9)° and 120.23(2)°, indicating that it is more compressed along the *c*-axis compared to those in $Yb_{14}MgBi_{11}$, which have bond angles of 105.62(1)° and 117.48(3) (6)°. This comparison shows that the Zn analog is the most compressed, while the Mg analog is the least compressed.

Unlike the lighter and smaller pnictogens P and As, the Bi analogs of 14-1-11 compounds show no split in the $Pn_3^{7-}$ unit. The Bi-Bi bond in the $Bi_3^{7-}$ subunit of $Yb_{14}ZnBi_{11}$ is 3.33 Å, which is comparable to $Yb_{14}MnBi_{11}$ (3.33 Å) but smaller than $Yb_{14}MgBi_{11}$ (3.35 Å). Lastly, Bi-Yb bond lengths in $Yb_{14}ZnBi_{11}$ are 3.2761(7) Å for Bi(1)-Yb(1) and 3.2225(8) Å for Bi(1)-Yb(4). In comparison, the longest and smallest Bi-Yb bond lengths in $Yb_{14}MnBi_{11}$ are 3.383(1) Å and 3.222(1) Å, respectively. For the Mg analog, they are 3.291(1) Å and 3.205(1) Å, indicating small differences in the range of 0.09 Å for the Bi-Yb bonds among these Bi-containing 14-1-11 compounds.

**Table 1** Data collection parameters and crystallographic data for flux-grown $Yb_{14}ZnBi_{11}$.

| | | |
|---|---|---|
| Temperature | 90(2) K | 200(2) K |
| Formula weight | 4786.71 g $mol^{-1}$ | |
| Crystal dimension | 0.141 x 0.069 x 0.067 $mm^3$ | 0.17 x 0.11 x 0.08 $mm^3$ |
| Wavelength | Mo, 0.71073 Å | |
| Crystal system | Tetragonal | |
| Space group | $I4_1/acd$ (no. 142) | |
| *a* | 16.9937(6) Å | 17.0232(13) Å |
| *c* | 22.1377(11) Å | 22.185(2) Å |
| *V* | 6393.1(6) $Å^3$ | 6429.0(10) $Å^3$ |
| Z | 8 | |
| Density (calculated) | 9.95 g $cm^{-3}$ | 9.89 g $cm^{-3}$ |
| Absorption coefficient | 1014.9 $cm^{-1}$ | 1009.3 $cm^{-1}$ |
| Theta range for data collection | 2.40 to 27.50° | 2.39 to 26.39° |

| Reflections collected | 17229 | 10118 |
|---|---|---|
| Independent reflections | 1844 [R(int) = 0.0823] | 1656 [R(int) = 0.0908] |
| Absorption correction | Empirical, SADABS (multi-scan) | |
| Max. and min. transmission | 0.1512 and 0.0282 | 0.1517 and 0.0812 |
| Goodness-of-fit (GOF) on $F^2$ | 1.122 | 1.085 |
| Final $R$ indices [$I > 2\sigma(I)$] | $R_1 = 0.0269$, $wR_2 = 0.0553$ | $R_1 = 0.0422$, $wR_2 = 0.0690$ |
| $R$ indices (all data) | $R_1 = 0.0335$, $wR_2 = 0.0573$ | $R_1 = 0.0608$, $wR_2 = 0.0741$ |

[a] $R_1 = \sum||F_o| - |F_c||/\sum|F_o|$; $wR_2 = [\sum[w(F_o^2 - F_c^2)^2]/\sum[w(F_o^2)^2]]^{1/2}$, where $w = 1/[\sigma^2F_o^2 + (AP)^2 + (BP)]$ and $P = (F_o^2 + 2F_c^2)/3$. $A$ and $B$ are the respective weight coefficients (see the CIF data).

### 3.2 Powder Synthesis

Polycrystalline $Yb_{14}ZnBi_{11}$ was synthesized by the powder metallurgy method through ball milling and high-temperature annealing. The powder X-ray diffraction (PXRD) pattern of $Yb_{14}ZnBi_{11}$ indicates all major Bragg peaks are well indexed with the simulated pattern from the crystallographic information file (CIF) generated from single-crystal synthesis, as shown in **Fig. 2**. The powder diffraction pattern shows impurity peaks around $2\theta$ = 27° and 31°. This has previously been observed in other bismuth-containing compounds and is attributed to the presence of a small amount of Bi.[21,22] The diffraction patterns were analyzed using Rietveld refinement with the GSAS-II software package, as shown in **Fig. S1**.[31] However, the broad peak could not be fitted to any crystalline form of Bi due to its amorphous nature. The PXRD patterns for synthesizing $Yb_{14}ZnBi_{11}$ at various temperatures, including excess Zn at 800 °C, are shown in the **SI**, **Fig. S2** and **S3**. Excess Zn increases the counts for the impurity peaks, suggesting a Zn-Bi or Yb-Zn-Bi phase; however, we were unable to find a published structure that fit these reflections. Therefore, we further characterized the sample with the lower-intensity impurity peaks. Further work is necessary to determine the impurity phase. The unit cell parameters from refinement are $a$ = 17.04786(22) Å, $c$ = 22.2117(4) Å, $V$ = 6455.37(16) Å$^3$. The differences in the lattice parameters from the single-crystal data are attributed to the difference in temperature during data collection, as the PXRD was collected at room temperature. In contrast, the CIF data for the single crystal were obtained at lower temperatures.

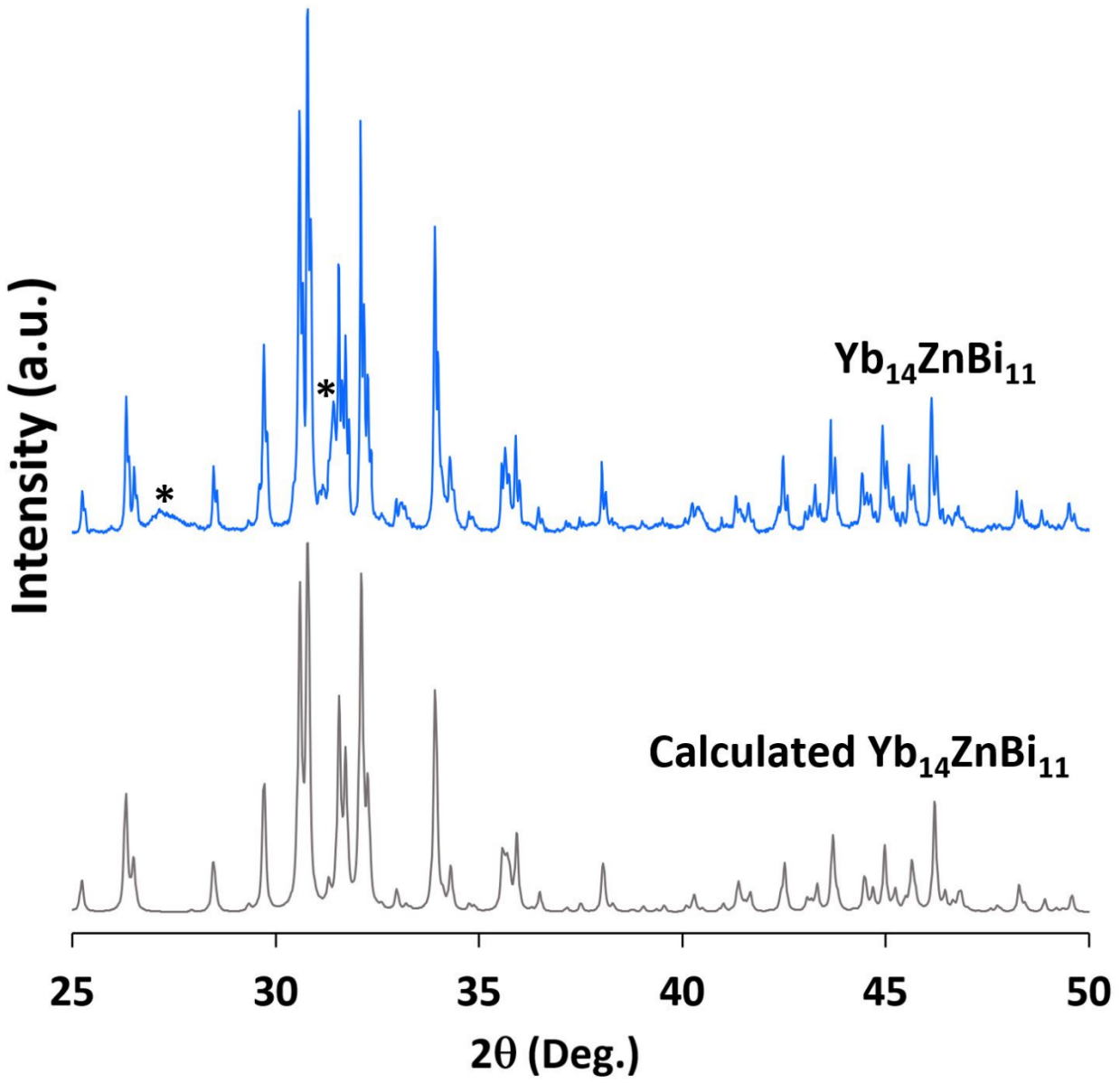



**Fig. 2** Room-temperature PXRD pattern of polycrystalline $Yb_{14}ZnBi_{11}$ sample. Impurity peaks marked by asterisks (*).

The SEM images and corresponding EDS elemental map of the $Yb_{14}ZnBi_{11}$ sample are provided in the **SI**, **Fig. S4**. The backscattered image confirms the sample's uniformity and absence of a secondary phase, while the secondary electron image verifies its high density. The elemental maps demonstrate the uniform distribution of each element. The composition obtained from the EDS is detailed in the **SI**, **Table S4**.

### 3.3 Electronic Transport Properties

Fig. 3 (a) presents the electrical resistivity of $Yb_{14}ZnBi_{11}$ as a function of temperature. The resistivity increases only slightly with temperature, indicating that this compound exhibits metallic

behavior. Specifically, the resistivity starts at 0.91 mΩ cm at 367 K and rises to 1.11 mΩ cm at 980 K. This temperature dependence highlights the electrical transport properties of the material. The resistivity behavior resembles that of other bismuth-containing compounds in the 14-1-11 series, such as $Yb_{14}MgBi_{11}$ and $Yb_{14}MnBi_{11}$.[22] In contrast, the antimony-containing compound $Yb_{14}ZnSb_{11}$ exhibits higher resistivity and a more significant increase as the temperature rises.[17]

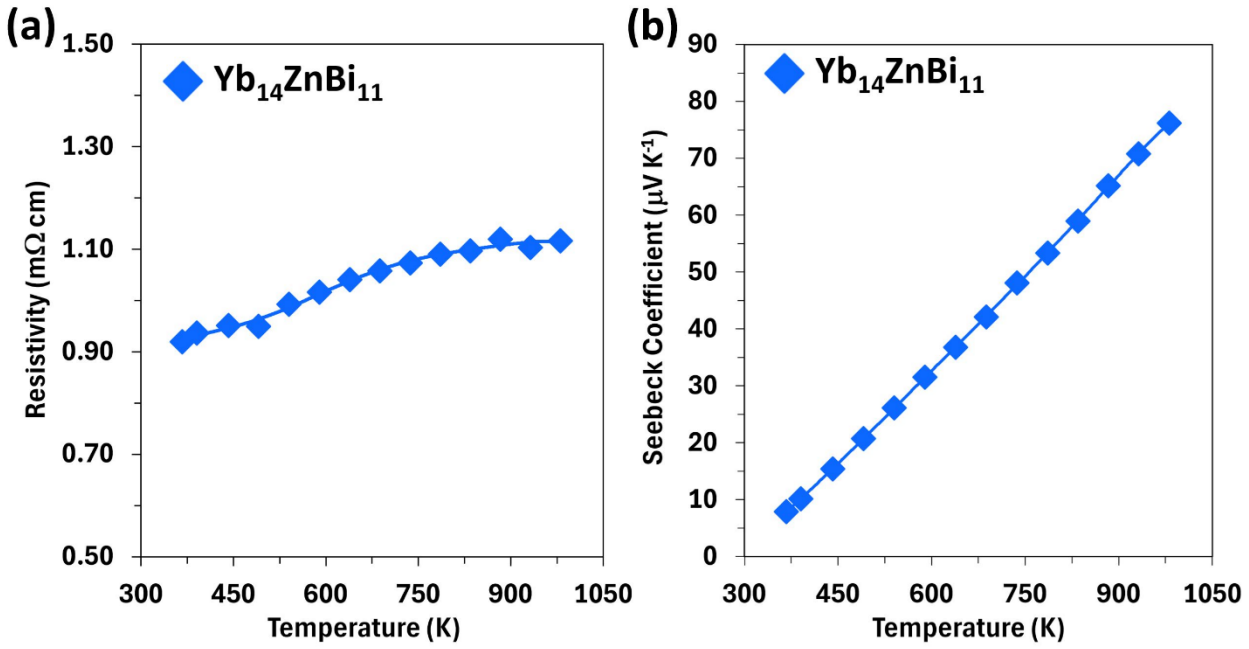



**Fig. 3** (a) Electrical resistivity and (b) Seebeck coefficient of $Yb_{14}ZnBi_{11}$ as a function of temperature.

The Seebeck coefficient of $Yb_{14}ZnBi_{11}$ increases with temperature, as illustrated in Fig. 3 (b). This increase, with positive values, indicates that the compound behaves like a *p*-type semiconductor. This behavior is similar to that of other bismuth-containing 14-1-11 analogs; however, the Seebeck coefficient of $Yb_{14}ZnBi_{11}$ is significantly lower than that of high-performing antimony analogs. This difference can be attributed to the electronic band structure of $Yb_{14}ZnBi_{11}$, as reported by Justl *et al.*[17] The energy offset between the first valence band maximum (light band) and the second valence band maximum (heavy band) is significant at 0.37 eV for $Yb_{14}ZnBi_{11}$. This results in only the lighter band, with a lower effective mass, contributing to the Seebeck coefficient. Another reason could be higher carrier concentrations in *p*-type semiconductors, leading to lower Seebeck coefficients, as carrier concentration and Seebeck coefficient are inversely proportional. The calculated bandgap of $Yb_{14}ZnBi_{11}$ has been reported to be 0.10 eV.[17] However, no bend over was observed in the Seebeck coefficient over the measured temperature range. This phenomenon has also been noted in other Bi-containing 14-1-11 compounds, including $Yb_{14}MnBi_{11}$,[22] $Yb_{14}MgBi_{11}$,[22] $Ca_{14}MgBi_{11}$,[21] and $Eu_{14}MgBi_{11}$.[21] The absence of a bipolar effect could be due to defects that keep the Fermi level deep within the valence band, preventing the activation of minority carriers. Alternatively, it may result from dispersion within the valence band coupled with

a relatively flat conduction band, where the mobility of majority carriers is significantly higher than that of minority carriers. Consequently, the contribution from minority carriers becomes negligible.[32] Extrapolating the experimental data to lower temperatures suggests that this compound may exhibit a negative Seebeck coefficient at low temperatures, indicating its potential as an *n*-type material.

### 3.4 Thermal Transport Properties

**Fig. 4** shows the temperature-dependent thermal conductivity of $Yb_{14}ZnBi_{11}$. The total thermal conductivity ($\kappa_T$) increases with rising temperature, indicating stronger thermal excitation of charge carriers at lower temperatures. At room temperature, the total thermal conductivity starts at 1.65 W $m^{-1}$ $K^{-1}$ and rises to 2.21 W $m^{-1}$ $K^{-1}$ at 1073 K. This level of thermal conductivity is higher than that of the antimony analogs of the 14-1-11 structure type, but comparable to other bismuth analogs. For example, $Yb_{14}MBi_{11}$ (*M* = Mg, Mn) exhibits a total thermal conductivity of approximately 1.4 W $m^{-1}$ $K^{-1}$ at room temperature and around 2.0 W $m^{-1}$ $K^{-1}$ at 875 K.[22]

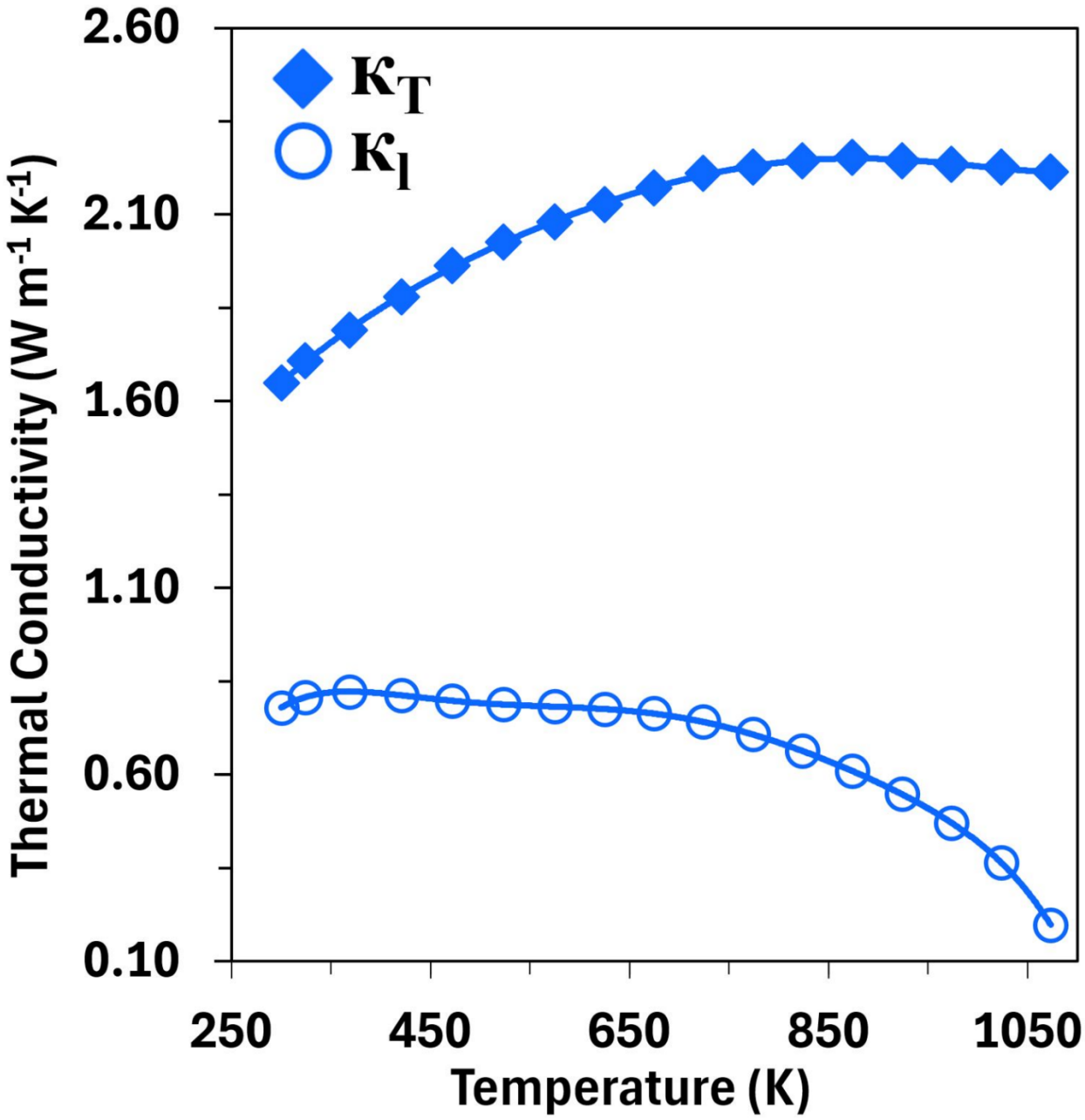



**Fig. 4** Temperature dependence of the total thermal conductivity ($\kappa_T$) and lattice thermal conductivity ($\kappa_l$) of $Yb_{14}ZnBi_{11}$.

To calculate the electronic thermal conductivity, the Wiedemann-Franz law is used, $\kappa_e = LT/\rho$. In this equation, $\rho$ is the electrical resistivity, $T$ is the temperature, and $L$ is the Lorentz number. The Lorentz number is determined using the Seebeck coefficient through the following equation.[33] The Lorentz number-temperature plot is provided in the **SI**, **Fig. S5 (a)**.

$$L = 1.5 + exp[-\frac{|S|}{116}]$$

The lattice thermal conductivity ($\kappa_l$) of 0.77 W $m^{-1}$ $K^{-1}$ at room temperature is relatively low, accounting for nearly 50 percent of the total conductivity. Thus, the high total thermal conductivity observed in $Yb_{14}ZnBi_{11}$ is primarily attributed to its electronic contribution. The electronic thermal conductivity as a function of temperature is shown in the **SI**, **Fig. S5 (b)**. This suggests that the carrier concentration, which affects electronic thermal conductivity, is quite high in this bismuth-containing compound. The lattice thermal conductivity does not exhibit the typical inverse relationship with temperature, represented as $T^{-1}$. This suggests that the Umklapp process is not the only factor influencing phonon transport; rather, a complex mechanism is at play, primarily governed by diffusion channels in addition to phonon channels.[19,20] Consequently, a close approximation of the theoretical minimum lattice thermal conductivity can be obtained only by considering both diffuson and phonon channels. For instance, theoretical lattice thermal conductivity has been reported for the Bi-containing Zintl compound $Yb_{14}MnBi_{11}$ by Hanus et al.[20]

The low lattice thermal conductivity in $Yb_{14}ZnBi_{11}$ can be attributed to the compound's complex structure and the large number of atoms (104 atoms per primitive cell). This trend is also observed in other 14-1-11 compounds.[13] There is a strong correlation between the number of atoms in a primitive cell and lattice thermal conductivity; generally, a greater number of atoms corresponds to lower lattice thermal conductivity.[34] For comparison, $Yb_{14}MnBi_{11}$ and $Yb_{14}MgBi_{11}$ have lattice thermal conductivities of 0.60 W $m^{-1}$ $K^{-1}$ and 0.20 W $m^{-1}$ $K^{-1}$, respectively, at room temperature. The slightly higher lattice thermal conductivity of $Yb_{14}ZnBi_{11}$ can be attributed to the mass ratio in the structure.[35] A smaller mass ratio results in higher lattice thermal conductivity, and in this case, the mass ratio of Bi to Zn is the smallest at 3. In contrast, the mass ratios of Bi to Mn and Bi to Mg are 4 and 8, respectively. Another contributing factor may be that the Zn-Bi bond is the least polarized. Zn has the highest electronegativity among these three metals, making the Zn-Bi bond more covalent. The comparatively shorter bond length of Zn-Bi at 2.7901(5) Å also indicates covalent bonding within the tetrahedron formed between the metal center and the pnictogen, leading to a higher lattice thermal conductivity.

### 3.5 Thermoelectric Efficiency

The thermoelectric figure of merit, $zT$, of $Yb_{14}ZnBi_{11}$ as a function of temperature is presented in **Fig. 5**. The $zT$ of $Yb_{14}ZnBi_{11}$ reaches a value of 0.22 at 973 K, showing the potential for further optimization of this compound by reducing the carrier concentration. In comparison to other reported bismuth-containing 14-1-11 compounds, the Zn analog exhibits lower thermoelectric efficiency due to its significantly higher total thermoelectric conductivity. However, the lattice thermal conductivity and resistivity are relatively low, which creates an opportunity to optimize the carrier concentration to improve thermoelectric efficiency.[15] Furthermore, the transport data indicate the presence of thermally activated carriers at low temperatures, suggesting the influence of grain boundary resistance. Implementing strategic grain boundary engineering could also enhance this compound's thermometric performance. This approach was recently demonstrated by Zavanelli *et al*. for 14-1-11 antimonides.[36]

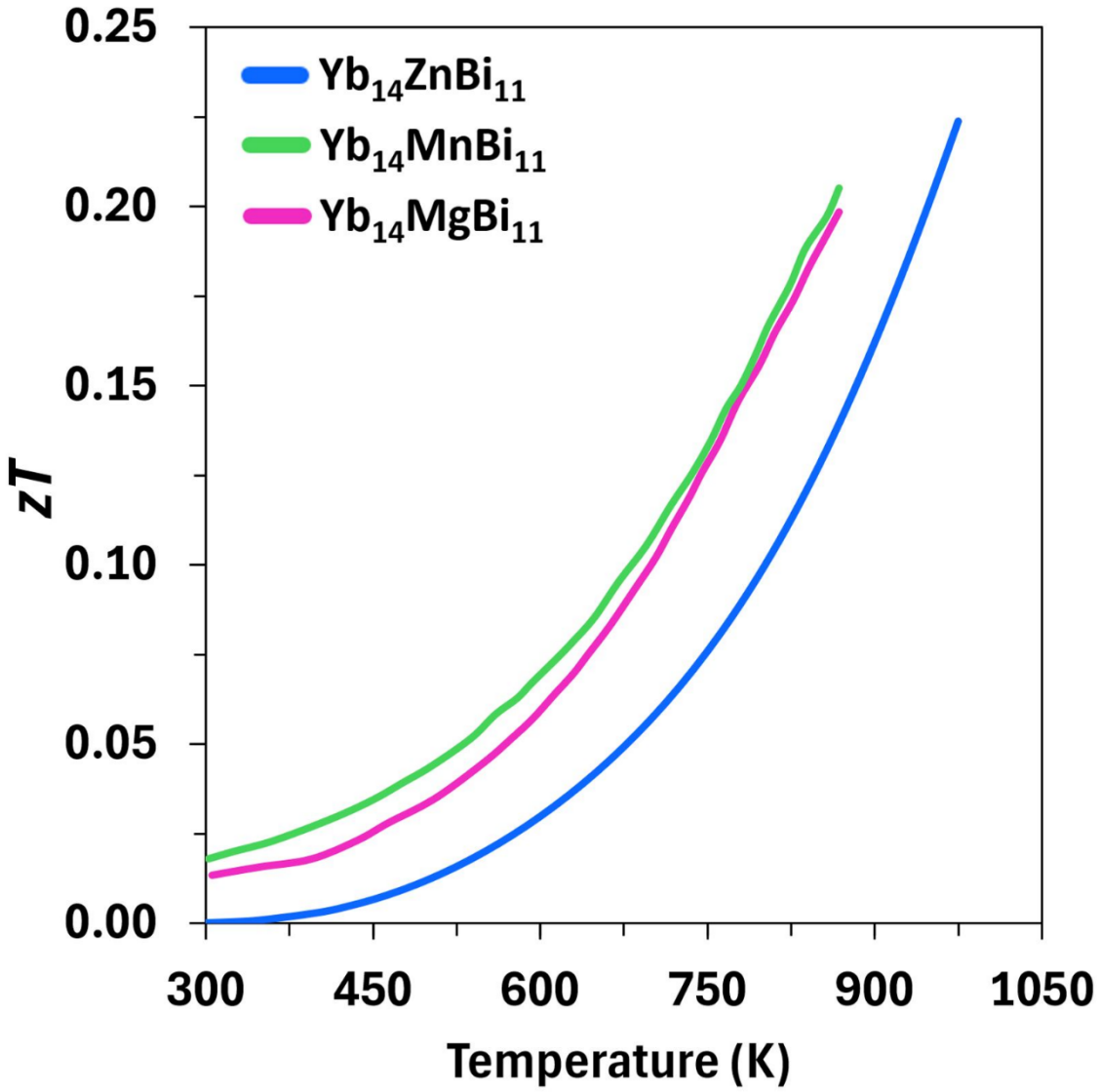



**Fig. 5** The dimensionless thermoelectric figure of merit, *zT*, as a function of temperature for $Yb_{14}ZnBi_{11}$ compared with reported data for $Yb_{14}MnBi_{11}$ and $Yb_{14}MgBi_{11}$.[22]

## 4 Conclusion

A new member of the Zintl 14-1-11 family, $Yb_{14}ZnBi_{11}$, has been synthesized as single crystals using the lead-flux method. This compound is a small bandgap semiconductor, exhibiting metallic behavior with very low resistivity and low lattice thermal conductivity. The addition of this compound to the 14-1-11 phases indicates that more materials in this family with heavier pnictogens should have potential applications in thermoelectricity. One notable feature of this compound is the Zn-Bi bond within its tetrahedral subunit, which has a relatively short bond length of 2.7901(5) Å. This shorter bond length results in a higher lattice thermal conductivity than that of other bismuth-containing compounds reported to date. The electronic contribution to thermal conductivity, calculated using the Wiedemann-Franz law, significantly affects the total thermal

conductivity, making it comparatively high. This also indicates a high concentration of charge carriers, which results in a low Seebeck coefficient. Moreover, the presence of amorphous bismuth may influence these properties. This suggests potential for optimizing thermoelectric performance by adjusting the high concentration of charge carriers. Furthermore, the low-temperature thermal excitation of charge carriers suggests that grain boundary engineering could also be an effective strategy for enhancing thermoelectric performance. In conclusion, the diverse family of Zintl phases remains promising for discovering new compositions useful for various applications.

## 5 Supporting Information

Deposition Numbers CCDC 2557387 (90 K), 2558874 and 2558875 (200 K) contain the supplementary crystallographic data for this paper. These data can be obtained free of charge via the joint Cambridge Crystallographic Data Centre (CCDC) and Fachinformationszentrum Karlsruhe Access Structures service/

Tables of $Yb_{14}ZnBi_{11}$ (90 K) atomic and displacement parameters, selected bond distances and angles, Table of EDS for the $Yb_{14}ZnBi_{11}$ pellet, Rietveld refinement of the polycrystalline sample, PXRD patterns of the polycrystalline product at different temperatures and excess Zn, SEM/EDX image for the pressed pellet, Plots of temperature dependent Lorentz number and electronic thermal conductivity. PDF

## 6 Acknowledgments

This work was supported by the National Science Foundation, DMR-2307231. The authors are grateful to the UC Davis Center for Nano and Micro Manufacturing (CNM2). Work at the University of Delaware was supported by the United States Department of Energy, Office of Science, Basic Energy Sciences, under Award #DE-SC0008885. The authors thank Dr. J. P. A. Makongo and Dr. K. Ghosh (University of Delaware) for their work on Yb-Zn-Bi compounds that led to the first identification of $Yb_{14}ZnBi_{11}$.

## 7 References

1. S. M. Kauzlarich, *Chemistry of Materials*, 2023, **35**, 7355-7362.
2. M. Ishtiyak, S. R. Watts, O. Pokhvata, T. Kandabadage and S. Baranets, *Zeitschrift für anorganische und allgemeine Chemie*, 2025, **651**, e202500070.
3. S. M. Kauzlarich, S. R. Brown and G. Jeffrey Snyder, *Dalton Transactions*, 2007, DOI: 10.1039/B702266B, 2099-2107.
4. L. Wu and V. L. Deringer, *Angewandte Chemie International Edition*, 2026, **65**, e08305.
5. J. A. Brehm, *Journal of Materials Chemistry C*, 2018, **6**, 1470-1475.
6. P. Gorai, A. Goyal, E. S. Toberer and V. Stevanović, *Journal of Materials Chemistry A*, 2019, **7**, 19385-19395.
7. M. M. Islam, M. Wróblewska, Y. Xu, E. S. Toberer and S. M. Kauzlarich, *Journal of Materials Chemistry A*, 2026, **14**, 8602-8609.

8. K. Ghosh, L. Borgsmiller, S. Baranets, G. J. Snyder and S. Bobev, *Journal of Materials Chemistry A*, 2024, **12**, 25416-25428.
9. S. Chanakian, A. Zevalkink, U. Aydemir, Z. M. Gibbs, G. Pomrehn, J.-P. Fleurial, S. Bux and G. J. Snyder, *Journal of Materials Chemistry A*, 2015, **3**, 10289-10295.
10. A. K. Hauble, M. Y. Toriyama, S. Bartling, A. M. Abdel-Mageed, G. J. Snyder and S. M. Kauzlarich, *Chemistry of Materials*, 2023, **35**, 7719-7729.
11. C. Miramontes Ruiz, M. Wróblewska, E. S. Toberer and S. M. Kauzlarich, *ACS Applied Energy Materials*, 2026, DOI: 10.1021/acsaem.6c00664.
12. R. Chaliha, M. Kothakonda, C.-W. Lee, J. N. Law, Q. Yang, S. Bobev and P. Gorai, *Journal of Materials Chemistry A*, 2025, **13**, 33385-33396.
13. Y. Hu, G. Cerretti, E. L. Kunz Wille, S. K. Bux and S. M. Kauzlarich, *Journal of Solid State Chemistry*, 2019, **271**, 88-102.
14. S. Baranets, G. M. Darone and S. Bobev, *Journal of Solid State Chemistry*, 2019, **280**, 120990.
15. H. Han, L. Zhao, X. Wu, B. Zuo, S. Bian, T. Li, X. Liu, Y. Jiang, C. Chen, J. Bi, J. Xu and L. Yu, *Journal of Materials Chemistry A*, 2024, **12**, 24041-24083.
16. W. Kim, *Journal of Materials Chemistry C*, 2015, **3**, 10336-10348.
17. A. P. Justl, F. Ricci, A. Pike, G. Cerretti, S. K. Bux, G. Hautier and S. M. Kauzlarich, *Science Advances*, 2022, **8**, eabq3780.
18. M. M. Islam, M. Wróblewska, Y. Xu, E. S. Toberer and S. M. Kauzlarich, *Journal of Materials Chemistry A*, 2026, DOI: 10.1039/D5TA09465H.
19. M. M. Islam, J. Zheng, A. Pike, K. E. Star, S. K. Bux, G. Hautier and S. M. Kauzlarich, *Journal of the American Chemical Society*, 2025, **147**, 42883-42893.
20. R. Hanus, J. George, M. Wood, A. Bonkowski, Y. Cheng, D. L. Abernathy, M. E. Manley, G. Hautier, G. J. Snyder and R. P. Hermann, *Materials Today Physics*, 2021, **18**, 100344.
21. W. Tan, Z. Wu, M. Zhu, J. Shen, T. Zhu, X. Zhao, B. Huang, X.-t. Tao and S.-q. Xia, *Inorganic Chemistry*, 2017, **56**, 10576-10583.
22. Y. Hu and S. M. Kauzlarich, *Dalton Transactions*, 2017, **46**, 3996-4003.
23. Q. Yan and M. G. Kanatzidis, *Nature Materials*, 2022, **21**, 503-513.
24. S.-Q. Xia and S. Bobev, *Journal of the American Chemical Society*, 2007, **129**, 10011-10018.
25. N.-T. Suen, Y. Wang and S. Bobev, *Journal of Solid State Chemistry*, 2015, **227**, 204-211.
26. S. Baranets and S. Bobev, *Inorganic Chemistry*, 2019, **58**, 8506-8516.
27. A. He, E. L. K. Wille, L. M. Moreau, S. M. Thomas, J. M. Lawrence, E. D. Bauer, C. H. Booth and S. M. Kauzlarich, *Physical Review Materials*, 2020, **4**, 114407.
28. I. R. Fisher, S. L. Bud'ko, C. Song, P. C. Canfield, T. C. Ozawa and S. M. Kauzlarich, *Physical Review Letters*, 2000, **85**, 1120-1123.
29. J. Y. Chan, M. M. Olmstead, S. M. Kauzlarich and D. J. Webb, *Chemistry of Materials*, 1998, **10**, 3583-3588.
30. Y. Hu, J. Wang, A. Kawamura, K. Kovnir and S. M. Kauzlarich, *Chemistry of Materials*, 2015, **27**, 343-351.
31. B. H. Toby and R. B. Von Dreele, *Journal of Applied Crystallography*, 2013, **46**, 544-549.
32. J. Qiu, S. Zhi, P. Zhao, J. Wang, X. Ma, S. Ye, C. Lin, X. Zhang, Z. Wu, S. Duan, H. Yao, F. Cao, Q. Zhang and J. Mao, *Physical Review B*, 2025, **111**, 045203.
33. H.-S. Kim, Z. M. Gibbs, Y. Tang, H. Wang and G. J. Snyder, *APL Materials*, 2015, **3**.
34. M. K. Jana and K. Biswas, *ACS Energy Letters*, 2018, **3**, 1315-1324.

35. D. T. Morelli and G. A. Slack, in *High Thermal Conductivity Materials*, eds. S. L. Shindé and J. S. Goela, Springer New York, New York, NY, 2006, DOI: 10.1007/0-387-25100-6_2, pp. 37-68.
36. D. Zavanelli, E. Isotta, F. Busch, S. Zhang, C. Scheu, S. Bux and G. J. Snyder, *Journal of Materials Chemistry A*, 2026, **14**, 11284-11293.